Structural and magnetic characterization of barbosalite Fe3(PO4)2(OH)2

M. Poienar, F. Damay, J. Rouquette, S. Malo, A. Maignan, E. Elkaim, Julien Haines, C. Martin

Structural and magnetic characterization of barbosalite Fe₃(PO₄)₂(OH)₂

M. Poienar[1], F. Damay[2], J. Rouquette[3], V. Ranieri[3], S. Malo[4], A. Maignan[4*],

E. Elkaïm[5], J. Haines[3] and C. Martin[4]

[1] *National Institute for Research and Development in Electrochemistry and Condensed Matter, Renewable Energies - Photovoltaic Laboratory, Str. Dr. A. Păunescu Podeanu, nr.144, 300569 Timişoara, Timiş, Romania*

[2] *Laboratoire Léon Brillouin, CEA-CNRS UMR 12, 91191 GIF-SUR-YVETTE CEDEX, France*

[3] *Institut Charles Gerhardt UMR CNRS 5253, Université Montpellier II, Place Eugène Bataillon, cc1503, 34095 Montpellier Cedex 5, France.*

[4] *Laboratoire CRISMAT, Normandie Univ, ENSICAEN, UNICAEN, CNRS, 14000 Caen, France*

[5] *Synchrotron Soleil, L'Orme des Merisiers, Saint-Aubin BP 4891192 GIF-sur-YVETTE CEDEX*

*corresponding author antoine.maignan@ensicaen.fr

Abstract

Single crystals and polycrystalline samples of barbosalite Fe₃(PO₄)₂(OH)₂ iron phosphate were successfully synthesized by hydrothermal method at low pressure and temperature. Careful investigations of the crystal structure by high resolution X-ray diffraction and transmission electron microscopy evidence a complex barbosalite framework where trimers of face sharing FeO₆ octahedra along the <110> direction are connected by an additional Fe site, partly occupied. Despite this structural disorder, the spins order in a rather simple magnetic structure below 160 K. The corresponding magnetic point group of $P2_1$ makes the barbosalite a promising candidate for the design of new multiferroics.

Keywords: barbosalite, crystal structure, magnetic order.

Introduction

Natural iron hydroxyl phosphates are minerals with a very rich crystal chemistry in connection with complex structures that are able to adapt several contents of Fe, OH or H_2O. The study of such materials, to determine their compositions and to establish relationships between structures, microstructures and functionalities, is often motivated by their applications related to energy and catalysis. For instance, $Li_3Fe_2(PO_4)_3$ or $LiFePO_4$ used as cathode materials in batteries have attracted much attention, according to the Li insertion made possible by the Fe^{3+}/Fe^{2+} redox couple [1-4]. In that respect, the $Fe_3(PO_4)_2(OH)_2$ barbosalite, belonging to the $P2_1/c$ $MgAl_2(PO_4)_2(OH)_2$ lazurite group, has just been recently shown to be less performing than $LiFePO_4$ with the possibility to exchange only 0.7 Li at 2.6V [5]. However, barbosalite exhibits the best catalytic properties of the Fe-P-OH-H system [6,7].

The presence of high spin Fe^{3+}/Fe^{2+} cations in these compounds make them interesting candidates for magnetoelectric properties. $LiFePO_4$, a member of the $LiMPO_4$ olivines, is an antiferromagnet with $T_N \approx 50K$ [8,9] that crystallizes in the same structure as the magnetoelectric members $LiNiPO_4$ and $LiCoPO_4$ [10,11]. In that context, it becomes worthy to study the magnetic structure of the $Fe_3(PO_4)_2(OH)_2$ barbosalite. This is also motivated by the presence in this structure of Fe trimers formed by face-shared FeO_6 octahedra [12,13]. Indeed, the presence of such trimers, in which a ferrous cation is surrounded by two ferric cations, could be involved in the multiferroic behaviour of the Fe_3BO_5 ludwigite [14].

G.J. Redhammer *et al.* [15] have reinvestigated the barbosalite and characterized its magnetic properties, revealing a magnetic transition at $\cong 160$ K, but the magnetic structure and its temperature dependence are still unknown. In this context, we have undertaken a detailed study of the $Fe_3(PO_4)_2(OH)_2$ barbosalite for its structural and magnetic properties, by using X-ray, neutron and electron diffraction and magnetometry, on both single crystals and polycrystalline samples.

Experimental section

Two types of hydrothermal synthesis were used, leading to barbosalite crystals with different sizes but with similar structural and physical properties.

(i) The reactants $FeCl_2 \cdot 4H_2O$ [1.2096 g], $FeCl_3$ [0.9869 g] and $(NH_4)_2HPO_4$ [0.8034 g] were dissolved independently in distilled water by magnetic stirring during 30 minutes approximatively. The mixtures were transferred to a 63 mL Teflon-lined stainless steel autoclave (80% degree of filling) and magnetically stirred at room temperature leading to the

formation of a greyish blue precipitate. Lastly, the autoclave was sealed and heated at 220ºC for 72 hrs. At the end, black green powder was collected by filtration, washed with distilled water and dried at 90ºC for 3 hrs in air.

(ii) $Fe_3(PO_4)_2(OH)_2$ single crystals of about 5-30 μm dimensions were grown hydrothermally at low pressure and 220°C from a mixture of $FeSO_4.7H_2O$ [7g], $FePO4.7H_2O$ [2.8g] and H_3PO_4 (85%) [2mL] (for 25mL d'H_2O and 60% degree of filling of the 45 mLTeflon-lined autoclave) which was quenched after one week

Room temperature (RT) X-ray powder diffraction (XRPD) data have been collected using a PANAlytical diffractometer with Co Kα radiations [5° < 2θ < 115°]. Room temperature synchrotron X-ray powder diffraction (SXRPD) was carried out on the CRISTAL beamline at SOLEIL, using a wavelength λ= 0.72613Å. A small amount of sample was crushed and sifted at 63μm and put in a 0.3mm quartz capillary. Neutron powder diffraction versus temperature was performed at LLB on the G4.1 diffractometer (λ = 2.428Å) from 1.7 to 300K. Rietveld refinements were performed by means of the Fullprof suite [16], which also includes the BasIreps software used for the representational analysis of the magnetic structure.

A 5 x 6 x 15 μm³ octahedral crystal was characterized by X-ray diffraction. Complete sphere-scans with a step width of 0.5° were performed with a Dectris Pilatus detector placed at 34 mm from the sample. Data collection, indexing, reduction and correction for absorption were performed using CrysAlisPro (Oxford Diffraction). Structure determination and refinements were performed using SHELXL-2014/7.31 [17]. WinGX was used for Fourier map.

Transmission electron microscopy (TEM) specimens were prepared by smoothly crushing samples with n-butanol in an agate mortar and depositing the drops onto a holey carbon grid supported by copper. Electron diffraction (ED) study at room temperature was carried out, using a JEOL 2010 microscope equipped with tilt-rotation sample holder (±50) (operating at 200 kV).

Magnetic properties were studied by collecting magnetization (M) in both zero-field-cooling (*zfc*) and field-cooling (*fc*) modes with a SQUID magnetometer (MPMS, Quantum Design) in a magnetic field of 100 Oe, from 5 to 300K. The magnetic susceptibility is calculated from these data. Magnetisation versus magnetic field loops were also collected by using the same equipment at 5, 50, 100, 150 and 180K, from 0 to +5T, then to -5T and then to +5T.

Results

Structural characterizations

The RT SXRPD pattern of the polycrystalline sample can be indexed using the $P2_1/n$ space group and lattice parameters: $a = 7.3231$Å, $b = 7.4687$Å, $c = 7.4073$Å and $\beta = 118.565°$, in agreement with the previous reports [5, 15]. The barbosalite framework is described as consisting of Fe^{3+}-Fe^{2+}-Fe^{3+} face sharing FeO_6 octahedra trimers, oriented along the <110> direction, and connected together by phosphate tetrahedra [15] (Figure 1a and 1b). In this model, two iron sites are necessary to build the structure: Fe1 in $4e$ Wyckoff position and Fe2 in $2a$ (0 0 0), corresponding to trivalent and divalent species, respectively (as determined from the average of the Fe-O distances). Fe2 sits at the inversion symmetry of the trimer. Although the refinement of the SXRPD data using this $P2_1/n$ space group lead to good agreement factors, very weak extra peaks were detected and attributed to a small amount of $Fe_4(PO_4)_3(OH)_3$ [18].

To go further in the structural analysis of $Fe_3(PO_4)_2(OH)_2$, numerous selected area electron diffraction (SAED) patterns were recorded on different crystallites and the reconstruction of the reciprocal space, carried out by tilting around the unique axis b^*, evidences a 2_1 screw axis along b and a lattice compatible with the parameters reported above (Figures 2a,b,c). But, whatever the crystallite, from single or poly-crystalline samples, none (0 1 0)* ED pattern is compatible with the existence of a n-glide plane (in Figure 2b the blue arrows point out the spots incompatible with a n-glide plane). The main spots are then compatible with the aforementioned lattice parameters and the $P2_1$ non centrosymmetric space group. Moreover, additional phenomena are observed, like twins as shown in Figure 2c or super lattice reflections as pointed out by blue arrows in the (1 0 0)* SAED pattern of Figure 3a. They are not well established and can vary slightly from a crystallite to another one leading to the formation of loci, sign of a state intermediate between short and long range orders. More often, extra spots are observed involving a doubling of the c parameter; the enlargement of the Figure 3b also evidences a small component perpendicular to the c-axis as the three extra spots are not perfectly aligned (Figure 3c). The existence of partly established order is also evidenced on the ($\bar{1}$ 1 2)* oriented SAED patterns within a same crystallite: patterns without extra spots (Figure 4a), patterns with extra spots implying a tripling of the cell along [0 2 -1]* (Figure 4b) or even patterns showing an overlap of zones with and without superstructures (Figure 4c) can be observed.

To take into account the TEM observations, symmetry was lowered to $P2_1$ and cell parameters were refined to $a = 7.3207(5)$ Å; $b = 7.4553(6)$ Å; $c = 7.4037(4)$ Å and $\beta =$

118.578(3)° (V = 354.849(4) Å^3). Lowering the symmetry to $P2_1$ involves three iron sites, instead of two, and the inversion centre at Fe2 is lost. The large number of parameters (3 Fe, 1P and 10 O -all in general (x, y, z) position) compared to the number and intensity of the "extra" Bragg peaks does not allow pushing further the analysis, which was pursued using single crystal SXRD data.

The diffraction data obtained on single crystals (sizes about 5 x 6 x 15 μm^3) exhibit good intensity, but poor diffraction quality, with signs of splitting/twinning in some images, in perfect agreement with the numerous defects observed by TEM. As mentioned above, the $P2_1/n$ has to be ruled out, as n-glide plane reflection conditions ($h0l$: $h+l=2n$) are violated, as observed also on the $h0l$ reconstruction of the reciprocal space, where additional super lattice reflections are clearly present, indicating a doubling along the c-axis (Figure 5). Synchrotron experiments performed also on larger crystals (sizes about $30 \times 15 \times 15$ μm^3) confirm the presence of these satellites but these data did not permit to solve the structure in the large cell, owing to poor crystal quality and low statistics of the hkl superlattice reflections. Consequently, the structure was solved in the $P2_1$ supercell, using the higher quality data of a chosen small crystal recorded at 175 K, leading to an agreement factor of 5.75% (Table 1). A polar twin was used giving rise to a Flack parameter of 0.55(5).

From single crystal data, the structure is refined as a supercell with a doubling of the c parameter within the $P2_1$ space group (Figure 1c). An additional Fe site, perfectly identifiable on the observed Fourier map (Figure 6), has to be introduced in the framework previously described. This latter Fe7 atom is partly occupied (22 %) and four over six other Fe sites are not fully occupied (Tables 2 and 3). Such a non-stoichiometric Fe7 site explains its anomalously large atomic displacement parameter (Table 2), and its highly distorted oxygen octahedral environment (Table 4). Hydrogen atoms are bonded to O9 and O15, which are both connected to three iron octahedra. Due to the existence of the nonstoichiometric Fe7, the two last hydrogens could not be placed on O12 and O8. Based on the structure refinement, the stoichiometry of the studied barbosalite crystal is found to be Fe$_{2.8(1)}$(PO$_4$)$_2$(OH)$_2$; as the residual electron density is rather high, the standard deviation of the iron content is however probably underestimated. Because of the extra nonstoichiometric iron site that statistically connects the trimers in the ab-plane, the structure can be described as derived from the $P2_1/n$ one with modulations of the Fe, P and O atomic positions, which can reach a magnitude of

0.027 Å. This additional Fe7 site statistically connects the trimers, as in the $P4_12_12$ lipscombite polymorph of barbosalite (Figure 1d).

In the ideal theoretical barbosalite structure, as already mentioned, there are two iron sites only, which are attributed to ferrous and ferric species regarding the average Fe-O distance of each octahedron. Those <Fe-O> reported in Table 4 for the studied crystal do not allow such a clear determination of the iron valence on the seven sites. The structural complexity revealed here by combining TEM and X-ray single crystal diffraction studies was not previously reported [5]. In any case, the refined structural parameters have to be taken cautiously. They correspond to the structure of one single crystal, because of the difficulty to find a crystal giving X-ray diffraction of reasonable quality and, owing to the disorder evidenced by electron diffraction, probably do not truly reflect the average structure.

Magnetic properties

The magnetic susceptibility curves (Figure 7a) show a magnetic transition at 164 K, below which there is a strong difference between the *zfc* and *fc* modes, in agreement with previous results [15]. The hysteretic behaviour of M(H) curves (Figure 7b) indicates ferromagnetic correlations up to 150 K (i.e.< T_N) with a very small remnant magnetization, less than 0.1 μ_B/f.u. (that is for 4 Fe).

The temperature dependence of the neutron diffractograms, recorded from 1.7 K to RT, shows no structural transition, within the instrumental resolution, but magnetic peaks appear below $\cong$ 160 K (Figure 8a). The corresponding evolutions of the unit cell parameters and volume (extracted from LeBail fitting using the $P2_1/n$ cell because of the reduced Q range) *vs.* temperature are small (<0.35%). The cell volume *V* decreases with decreasing temperature, and only a weak deviation from the Debye law is observed around T_N. In the same way, *a* and *c* decrease with temperature, in contrast with the negative thermal expansion (NTE) observed along the *b*-axis, the β angle remaining nearly constant (Figure 8b).

For the sake of simplicity, in the first stages of the analysis, the small $P2_1/n$ cell was used for the magnetic structure determination, to decrease the number of independent atoms in the magnetic cell. Below T_N = 160 K, the magnetic peaks can be indexed with the propagation vector **k** = 0 0 0. The resolution-limited width of the magnetic Bragg peaks attests of a well-established long range magnetic order. The corresponding magnetic structure at 1.5 K has been determined by Rietveld refinement using symmetry adapted modes derived from a representation analysis performed with the BasIreps program [16].

There are four one-dimensional irreducible representations of the little group G_k for $\mathbf{k}$ = 0 0 0. The magnetic representation Γ_m calculated for the Wyckoff positions of the two independent Fe atom in the $P2_1/n$ space group is $\Gamma_m = 3\Gamma_1 \oplus 3\Gamma_3$ for the 2a site and $\Gamma_m = 3\Gamma_1 \oplus 3\Gamma_2 \oplus 3\Gamma_3 \oplus 3\Gamma_4$ for the 4e site, so that there are three basis functions for each representation. Table 5 lists the corresponding basis vectors. The best models were obtained using the single Γ_1 irreducible representation for both sites, and mixing components along a and c. Although they belong to different Wyckoff sites, the moments of both Fe sites were constrained to be parallel, to limit the number of free parameters in the refinement, owing to the limited number of available magnetic peaks and to the additional difficulty of the $\mathbf{k}$ = 0 0 0 structure. The refinement was actually not improved significantly by releasing this constraint, in agreement with the random Fe^{2+}/Fe^{3+} distribution. Similarly, adding a magnetic component along b did not lead to quantifiably better results. The best refinement is illustrated in Figure 9a, with the corresponding magnetic structure in Figure 9b. The components of the magnetic moment are m_x = 1.5(1) μ_B and m_z = 4.8(1) μ_B, that is, nearly perpendicular to the ab plane (the deviation is ≈ 10°, Figure 9b). The ordered component maximum is close to 4.3 μ_B, i.e. in agreement with the theoretical value of 4.66 μ_B expected to a nominal $2Fe^{+3}:1Fe^{+2}$ composition taking the spin only value (5 μ_B and 4 μ_B for Fe^{+3} and Fe^{+2}, respectively). Since the magnetic structure is solved in the small $P2_1/n$ cell, the value of magnetic moment cannot be discussed further, in particular in link with the small remnant magnetization observed on the M(H) curves. Within iron trimers, moments are ferromagnetically coupled and surrounding trimers along c are aligned antiferromagnetically. This average model in the small $P2_1/n$ cell gives a very satisfactory refinement of the neutron diffraction data; lowering the symmetry to the $P2_1$ cell doubled along c with seven independent Fe atoms and unconstrained m_x, m_y, and m_z components leads to the magnetic space group $P2_1$ (BNS #4.7). Refinements of the individual m_x and m_z components (assuming m_y = 0) on each Fe sites were therefore not attempted, owing to the lack of information intrinsic to the powder data. In the larger barbosalite cell, the general picture of ferromagnetic planes of Fe trimers coupled AF along c remains the key feature of the magnetic ordering, with Fe moments arguably varying slightly depending on the site considered. Importantly, the magnetic point group of $P2_1$ allows non-zero polarisation and linear magneto-electric tensors, making of the barbosalite structure a promising candidate for the design of new multiferroics.

Discussion and conclusion

The monoclinic structure proposed initially for the barbosalite $Fe_3(PO_4)_2(OH)_2$ [15] is characterised by the existence of Fe^{3+}-Fe^{2+}-Fe^{3+} "trimers", also-called h-clusters, specific to iron phosphates materials [19], with short Fe-Fe equal distances within the trimers; those trimers are themselves connected by PO_4 tetrahedra, leading to a dense structural arrangement. In this structural framework, disorder is observed by TEM, with the existence and coexistence of several types of super structures and defects as twins. This is confirmed by a single crystal analysis showing a double cell with an extra Fe site, leading to a distribution of iron on seven crystallographic sites and thus to a distribution of Fe-O distances and probably to a distribution of iron valence states incompatible with Fe^{3+}-Fe^{2+} long range charge ordering.

This arrangement in clusters of face-sharing FeO_6 octahedra is common to barbosalite and lipscombite, which have the same composition. Barbosalite may be considered as an ordered equivalent of the $P4_12_12$ lipscombite, having "isolated" 3Fe-clusters instead of chains. Indeed, the lipscombite structure is composed of face sharing FeO_6 octahedra according to the scheme Fe1-Fe3-Fe2-Fe3-Fe1, with an occupancy factor of 0.47 for Fe1 and Fe2. As in barbosalite, the chains are interconnected by PO_4 tetrahedra [19,20] (Figure 1d). The fact that there is a close structural relationship between the barbosalite and lipscombite crystal structures is also further confirmed by the barbosalite to lipscombite transition observed when annealing in air.

The studied single crystal appears thus as an intermediate case between the perfect iron order and disorder of barbosalite and lipscombite, respectively. It is clear that several types of super cells exist, as demonstrated by TEM observations, which probably correspond to the stabilization of other iron distribution. The arrangement of iron face-sharing octahedra trimers, combined with a distribution of iron site occupancies, allows various lattices to be built. The complexity of the crystal chemistry of the iron phosphates was already underlined by P.B. Moore in 1970 [19]. It also explains why different chemical formula and symmetries have been reported in the literature for both natural and synthetic lipscombite samples for instance. More generally, the quaternary system FeO-Fe_2O_3-P_2O_5-H_2O is very rich and complex, due to the huge number of phases it contains and to the relationships between them [21,22].

Even if the description based on Fe-trimers for barbosalite and derived structures is pertinent, depending on the compounds the average sizes of FeO_6 octahedra and their distortions strongly vary, requiring spectroscopy for identification of the ferrous and ferric species. The OH group probably plays also a role on the ferric and ferrous cations ordering,

referring to the phases obtained after catalytic reaction that belong to the $Fe_{4+2x}(PO_4)_3(OH)_{3-3x}O_{3x}$ solid solution (with $0 \leq x \leq 1$) [6].

Concerning the magnetic ordering, the fact that long-range antiferromagnetism is evidenced in this study demonstrates that the structural complexity with 7 Fe sites not all fully occupied, detrimental to the charge ordering, has actually little impact on magnetic exchanges.

This strongly supports that Fe-O-Fe superexchange is strong in that compound.

Interestingly, in Fe_3BO_5, multiferroicity was preserved by Mn substitution, although Fe^{2+}-Fe^{+3} charge ordering was also suppressed [14]. The origin of the spontaneous polarisation which appears below T_N in the ludwigite compounds is still an open question, as it could be linked with a polar disorder of charges in the structure. In all cases, it would be interesting to measure the electrical polarisation of barbosalite as a function of temperature or/and magnetic field in order to check the magnetoelectric coupling predicted by the symmetry analysis of the magnetic structure.

References

[1] Chen J. Recent Progress in Advanced Materials for Lithium Ion Batteries. *Materials* **2013**, *6*, 156-183.

[2] Masquelier C.; Padhi A. K.; Nanjundaswamy K. S.; Goodenough J. B. New Cathode Materials for Rechargeable Lithium Batteries: The 3-D Framework Structures $Li_3Fe_2(XO_4)_3$ (X=P, As). *Journal of Solid State Chemistry* **1998**, *135*, 228-234.

[3] Nanjundaswamy K. S.; Padhi A. K.; Goodenough J. B.; Okada S.; Ohtsuka H.; Arai H.; Yamaki J. Synthesis, redox potential evaluation and electrochemical characteristics of NASICON-related-3D framework compounds. *Solid State Ionics* **1996**, *92*, 1-10.

[4] Padhi A. K.; Nanjundaswamy K. S.; Goodenough J. B. Phospho-olivines as Positive-Electrode Materials for Rechargeable Lithium Batteries *J. Electrochem. Soc.* **1997**, *144,* 1188-1194.

[5] Sandineni P.; Ghosh K; Choudhury A. Electrochemistry of Illusive Barbosalite, $Fe^{2+}Fe^{3+}_2(PO_4)_2(OH)_2$: An Iron Phosphate Related to Lipscombite Structure *J. Electrochem. Soc.* **2019**, 166, A3585.

[6] Rouzies D.; Millet J.M.M.; Siew Hew Sam D.; Vedrine J.C. Isobutyric acid oxidative dehydrogenation over iron hydroxyphosphates. I. Catalytic properties and role of water. *Applied Catalysis A*: *General* **1995**, *124,*189-203.

[7] Millet J. M. M.; Rouzies D.; Vedrine J.C. Isobutyric acid oxidative dehydrogenation over iron hydroxyphosphates. II. Tentative description of the catalytic sites based on Mossbauer spectroscopic study. *Applied Catalysis A: General* **1995**, *124*, 205-219.

[8] Rousse G.; Rodriguez-Carvajal J.; Patoux S.; Masquelier C. Magnetic Structures of the Triphylite $LiFePO4$ and of Its Delithiated Form $FePO4$, *Chem. Mater.* **2003,** *15*, 4082-4090

[9] Toft-Petersen R.; Reehuis M.; Jensen T. B. S.; Andersen N. H.; Jiying Li J.; Le M. D.; Laver M.; Niedermayer C., Klemke B., Lefmann K. ; Vaknin D. Anomalous magnetic structure and spin dynamics in magnetoelectric $LiFePO4$, *Phys. Rev. B: Condens. Matter* **2015,** *92*, 024404.

[10] Mercier M.; Gareyt J.; Bertaut E. F., Une nouvelle famille de corps magnetoélectriques $LiMPO4$ (M= Mn, Co, Ni) *C. R. Acad. Sci. Ser. B* **1967** 264, 979.

[11] Kornev I.; Bichurin M.; Rivera J-P.; Gentil S.; Schmid H.; Jansen A. G. M.; Wyder P. Magnetoelectric Properties of $LiCoPO4$ and $LiNiPO4$, *Phys. Rev. B: Condens. Matter* **2000,** *62*, 12247.

[12] Lindberg M.; Christ C. L. Crystal structures of the isostructural minerals lazulite, scorzalite and barbosalite. *Acta Cryst.* **1959**, *12*, 695-697.

[13] Rouzies D.; Millet J.M.M. Mossbauer spectroscopic study of synthetic lipscombite and barbosalite at room temperature. *Hyperfine Interactions* **1993,** *77*, 11-18.

[14] Maignan A.; Lainé F.; Guesdon A.; Malo S.; Damay F.; Martin C. Charge ordering and multiferroicity in Fe_3BO_5 and Fe_2MnBO_5 oxyborates *Journal of Solid State Chemistry* **2017**, 246, 209–213.

[15] Redhammer G. J.; Tippelt G.; Roth G.; Lottermoser W.; Amthauer G. Structure and Mossbauer spectroscopy of barbosalite $Fe^{2+}Fe^{3+}_2$ $(PO_4)_2(OH)_2$ between 80 K and 300 K. *Phys. Chem. Minerals* **2000**, *27*, 419-429.

[16] Rodriguez-Carvajal J., Recent advances in magnetic structure determination by neutron powder diffraction, *Phys. B: Condens. Matter* **1993,** *192*, 55-69

[17] Sheldrick, G. M. A short history of SHELX. *Acta Crystallogr., Sect. A: Found. Crystallogr.* **2008**, *64*, 112−122.

[18] Torardi C.C.; Reiff M.; Takacs I. Crystal Structure, and Magnetism of $Fe_4(OH)_3(PO_4)_3$ and $V_4O(OH)_2(PO4)_2$: Chains of M_2O_9 Dimers Connected by Hydroxyl Groups, *J. of Solid State Chemistry* **1989**, *82*, 203-215.

[19] Moore P. B. Crystal chemistry of the basic iron phosphate. *American Mineralogist* **1970,** *55*, 135-169.

[20] Vencato, I.; Mattievich, E.; Mascarenhas, Y. P. Crystal structure of synthetic lipscombite: A redetermination. *Am. Miner.* **1989**, *74*,456-460.

[21] P. Schmid-Beurmann Stability properties and phase relations of $Fe^{3+}_{4-x}Fe^{2+}_{3x}(PO_4)_3(OH)_{3-3x}O_{3x}$ in the quaternary system $FeO-Fe_2O_3-P_2O_5-H_2O$ *J. Mater. Chem.*, **2001**, 11, 660-667

[22] P. Schmid-Beurmann Synthesis and phase characterization of a solid solution series between $\beta-Fe_2(PO_4)O$ and $Fe_4(PO_4)_3(OH)_3$ *J. Solid State Chem.* **2000** 153, 237-247

Table 1: Crystal data with *P*2$_1$ space group.

	*P*2$_1$ (#4)
Sum formula	Fe$_{11.5}$O$_{40}$ P$_8$H$_4$
a(Å)	7.2878(13)
b(Å)	7.4749(9)
c(Å)	14.793(2)
β(°)	118.52(2)
V(Å^3)	708.1(2)
Z	2
μ /mm^{-1}	52.718
ρ$_{calc}$ /gcm^{-3}	3.5967
F(000)	742.6
2θ range /°	6.073 - 66.672
Index ranges	-8 ≤ h ≤ 8, -4 ≤ k ≤ 8, -17 ≤ l ≤ 16
no. of measured reflns no of unique	2511 [Rint = 0.016] 1361
Average I/σ	35.46
Data/Restraints/Parameters	2511/0/175
Final R factors [I>2σ (I)]%	5.75
Largest residual peak/hole /eÅ^{-3}	1.889/-0.97
Flack parameter	0.55(5)

Table 2: Crystallographic parameters [atomic coordinates (all atoms are in the general (x, y, z) 2a Wyckoff site), site occupancy factors (Occ), and equivalent isotropic (U_{eq}) atomic displacement parameters (Å^2)] of $Fe_3(PO_4)_2(OH)_2$ at 175K. Hydrogen atom generation was performed with OH distance = 0.98 Å and ADP arbitrarily fixed at 0.5 Å^2.

	x	y	z	Occ	U_{eq}
Fe1	0.4727(5)	0.4615(8)	0.1199(3)	0.93(2)	0.0096(10)
Fe2	0.7511(7)	0.7318(9)	0.6264(4)	0.85(2)	0.0068(8)
Fe3	0.5237(5)	0.9627	0.3785(3)	1	0.0144(10)
Fe4	-0.2478(7)	0.7302(8)	0.1272(3)	1	0.0150(8)
Fe5	0.9780(6)	0.4963(7)	0.3730(3)	0.85(2)	0.0085(10)
Fe6	0.0231(6)	0.9962(7)	0.1276(3)	0.91(2)	0.0094(9)
Fe7	1.250(5)	0.180(5)	0.628(3)	0.22(3)	0.078(9)
P1	0.2467(10)	0.8425(17)	-0.0020(4)	1	0.0155(15)
P2	0.7550(10)	0.3428(17)	0.5026(4)	1	0.0147(15)
P3	0.2520(12)	0.6127(14)	0.2533(4)	1	0.0120(13)
P4	0.7474(12)	0.1134(14)	0.2462(5)	1	0.0137(14)
O1	0.202(2)	0.957(3)	0.0676(12)	1	0.016(4)
O2	0.692(2)	0.456(2)	0.5730(11)	1	0.011(3)
O3	0.800(3)	0.458(3)	0.4346(13)	1	0.022(4)
O4	0.310(2)	0.956(2)	-0.0711(11)	1	0.010(3)
O5	0.448(2)	0.718(2)	0.3218(11)	1	0.009(3)
O6	0.552(2)	0.218(2)	0.1775(12)	1	0.012(3)
O7	0.926(3)	0.232(3)	0.3130(13)	1	0.020(4)
O8	0.726(3)	0.591(3)	0.2453(12)	1	0.010(4)
O9	0.724(3)	0.591(3)	0.7439(12)	1	0.012(4)
H1	0.6578	0.6764	0.7698	1	0.5
O10	0.073(2)	0.731(2)	0.1874(12)	1	0.014(4)
O11	0.567(2)	0.209(3)	0.4402(11)	1	0.011(3)
O12	0.762(3)	0.859(4)	0.5003(13)	1	0.028(5)
O13	0.430(2)	0.708(3)	0.0578(11)	1	0.013(3)
O14	0.183(3)	0.487(3)	0.3151(14)	1	0.027(4)
O15	0.227(3)	0.359(4)	-0.0077(13)	1	0.024(5)
H2	0.1618	0.2724	0.0178	1	0.5
O16	0.058(3)	0.722(3)	-0.0667(13)	1	0.021(4)
O17	0.942(3)	0.220(3)	0.5639(13)	1	0.020(4)
O18	0.303(2)	0.483(3)	0.1881(13)	1	0.020(4)
O19	0.815(3)	-0.012(3)	0.1858(13)	1	0.021(4)
O20	0.700(2)	-0.014(3)	0.3125(12)	1	0.015(4)

Table 3: Atomic displacement parameters of $Fe_2^{3+}Fe^{2+}(PO_4)_2(OH)_2$ corresponding to Table 2 (U_{ij} (Å^2)).

	U_{11}	U_{22}	U_{33}	U_{23}	U_{13}	U_{12}
Fe1	0.0081(16)	0.010(2)	0.0044(15)	-0.0031(15)	-0.002(2)	-0.002(2)
Fe2	0.0084(15)	0.0024(18)	0.0102(14)	0.0033(14)	0.0049(12)	0.0019(13)
Fe3	0.0133(17)	0.018(3)	0.0045(14)	-0.0051(15)	-0.002(2)	-0.004(2)
Fe4	0.0155(15)	0.0146(19)	0.0043(12)	-0.0021(13)	-0.004(1)	-0.002(1)
Fe5	0.0123(18)	0.002(2)	0.0143(18)	-0.0012(17)	0.0092(16)	-0.003(2)
Fe6	0.0098(16)	0.009(2)	0.0056(15)	-0.0016(16)	0.0006(14)	-0.001(2)
P1	0.014(3)	0.021(4)	0.010(3)	0.000(2)	0.005(2)	0.000(3)
P2	0.012(3)	0.024(4)	0.007(3)	-0.003(2)	0.004(2)	-0.003(3)
P3	0.015(3)	0.006(2)	0.008(2)	-0.001(2)	-0.002(2)	-0.003(3)
P4	0.015(3)	0.007(3)	0.014(3)	0.001(3)	0.003(2)	0.003(3)

Table 4: Interatomic distances (Å) corresponding to Table 2 (Fe and P are in octahedral (Oh) and tetrahedral (Td) environments, respectively), the average Fe-O distance in each octahedron is given in the last column.

Fe1	O18	O6	O15	O4	O13	O8	<2.019>
	1.942(17)	1.972(18)	2.03(2)	2.031(15)	2.016(19)	2.125(18)	
Fe2	O11	O14	O7	O9	O12	O2	<2.100>
	2.046(15)	2.05(2)	2.080(17)	2.118(19)	2.13(2)	2.174(18)	
Fe3	O20	O12	O5	O2	O11	O9	<2.002>
	1.956(16)	1.97(2)	1.977(17)	2.018(15)	2.010(18)	2.083(18)	
Fe4	O10	O13	O15	O19	O8	O4	<2.098>
	2.067(15)	2.070(15)	2.08(2)	2.07(2)	2.120(18)	2.179(18)	
Fe5	O17	O3	O8	O14	O7	O12	<2.031>
	1.87(2)	1.929(18)	2.032(19)	2.050(19)	2.125(19)	2.18(2)	
Fe6	O16	O1	O9	O19	O10	O15	<2.022>
	1.87(2)	1.921(16)	2.042(19)	2.071(17)	2.127(18)	2.10(2)	
Fe7	O3	O8	O5	O17	O12	O20	<2.078>
	1.84(4)	1.92(4)	1.98(3)	2.00(4)	2.29(4)	2.44(6)	
P1	O1	O13	O16	O4			
	1.488(19)	1.54(2)	1.556(17)	1.566(18)			
P2	O3	O17	O11	O2			
	1.48(2)	1.53(2)	1.570(17)	1.590(18)			
P3	O5	O10	O14	O18			
	1.518(17)	1.492(18)	1.55(2)	1.53(2)			
P4	O6	O7	O20	O19			
	1.516(18)	1.493(19)	1.52(2)	1.53(2)			

Table 5: Basis functions for axial vectors associated with irreducible representations Γ_1 for Wyckoff site 2*a* and 4*e* in $P2_1/n$ space group.

Γ_1	(x, y, z) Fe$_{11}$	$(-x+\frac{1}{2}, y+\frac{1}{2}, -z+\frac{1}{2})$ Fe$_{12}$		(x, y, z) Fe$_{21}$	$(x+\frac{1}{2}, y-\frac{1}{2}, -z+\frac{1}{2})$ Fe$_{22}$	$(-x+1, -y+1, -z+1)$ Fe$_{23}$	$(x+\frac{1}{2}, -y+3/2, -z+\frac{1}{2})$ Fe$_{24}$
ψ_1	(1 0 0)	(1 0 0)	ψ_1'	(1 0 0)	(-1 0 0)	(1 0 0)	(-1 0 0)
ψ_2	(0 1 0)	(0 1 0)	ψ_2'	(0 1 0)	(0 1 0)	(0 1 0)	(0 1 0)
ψ_3	(0 0 1)	(0 0 -1)	ψ_3'	(0 0 1)	(0 0 -1)	(0 0 1)	(0 0 -1)

Figure Captions

Figure 1. Barbosalite structure in the small $P2_1/n$ space group: (a) showing the PO_4 tetrahedra (yellow) and FeO_6 octahedra (red and orange) and (b) highlighting the Fe trimers. Double barbosalite structure in the $P2_1$ space group, the blue octahedra correspond to the additional Fe7 site (c). Lipscombite structure $P4_32_12$ (d).

Figure 2. SAED patterns recorded at RT on $Fe_3(PO_4)_2(OH)_2$ oriented $(100)^*$ (a), $(010)^*$ (b) and $(\bar{2}03)^*$ (c). The blue arrows on the $(010)^*$ pattern point out the spots incompatible with a n-glide plane. The green line on Figure 1c indicates a twinned plane.

Figure 3. SAED patterns recorded at RT on $Fe_3(PO_4)_2(OH)_2$ oriented $(100)^*$ (a), the blue arrows point out the loci due to partial ordering phenomena and $(010)^*$ (b), the blue ellipses surround extra reflections. Figure 2(c) is an enlargement of Figure 2(b).

Figure 4. $(\bar{1}\,1\,2)$ SAED patterns recorded at RT on $Fe_3(PO_4)_2(OH)_2$, without ordering phenomena (a), implying a tripling along $[0\,2\,\bar{1}]^*$ (b) and with an overlap of ordered and non-ordered domains (c).

Figure 5. h0l and 0kl reconstructions of reciprocal space. Reflections (with h+l=2n+1) excluding the possibility of $P2_1/n$ space group and $1 \times 1 \times 2$ superlattice reflections (SR) are highlithed.

Figure 6. (a) Observed Fourier map at y = 0.16 with the $P2_1$ crystal structure showing the existence of the Fe07 site. Color scale is in $e^-Å^{-3}$

Figure 7. (a) Evolution with temperature of the magnetic susceptibility $\chi(T)$ of $Fe_3(PO_4)_2(OH)_2$, recorded in 100 Oe in zfc and fc modes, the magnetic ordering temperature is evidenced by a vertical arrow. (b) Magnetization curves at 5 K, 50 K, 100 K, 150 K and 180 K.

Figure 8. (a) Neutron powder diffraction patterns of barbosalite *vs.* temperature, from 1.5 to 300 K (λ= 2.427Å, G4.1 diffractometer at LLB) (top). Superposition of the corresponding 1.5 and 300 K patterns (bottom).

(b) Relative evolution of unit cell parameters for barbosalite from neutron diffraction data ($P2_1/n$ space group) between 1.5 K and 300 K.

Figure 9. (a) Rietveld refinement results (experimental data: open circles, calculated profile : continuous line, allowed Bragg reflections : vertical marks. The first and second rows of marks correspond to the crystal and magnetic Bragg peak positions, respectively. The difference between the experimental and calculated profiles is displayed at the bottom of the graph.) of the 1.5 K neutron diffraction data (G4.1) of $Fe_3(PO_4)_2(OH)_2$. (b) Corresponding magnetic structure of $Fe_3(PO_4)_2(OH)_2$ at 1.5 K.

Figure 1

(a)

(b)

(c)

(d)

18

Figure 2.

(a)

(b)

(c)

Figure 3.

(a)

(b)

(c)

Figure 4.

(a)

(b)

(c)
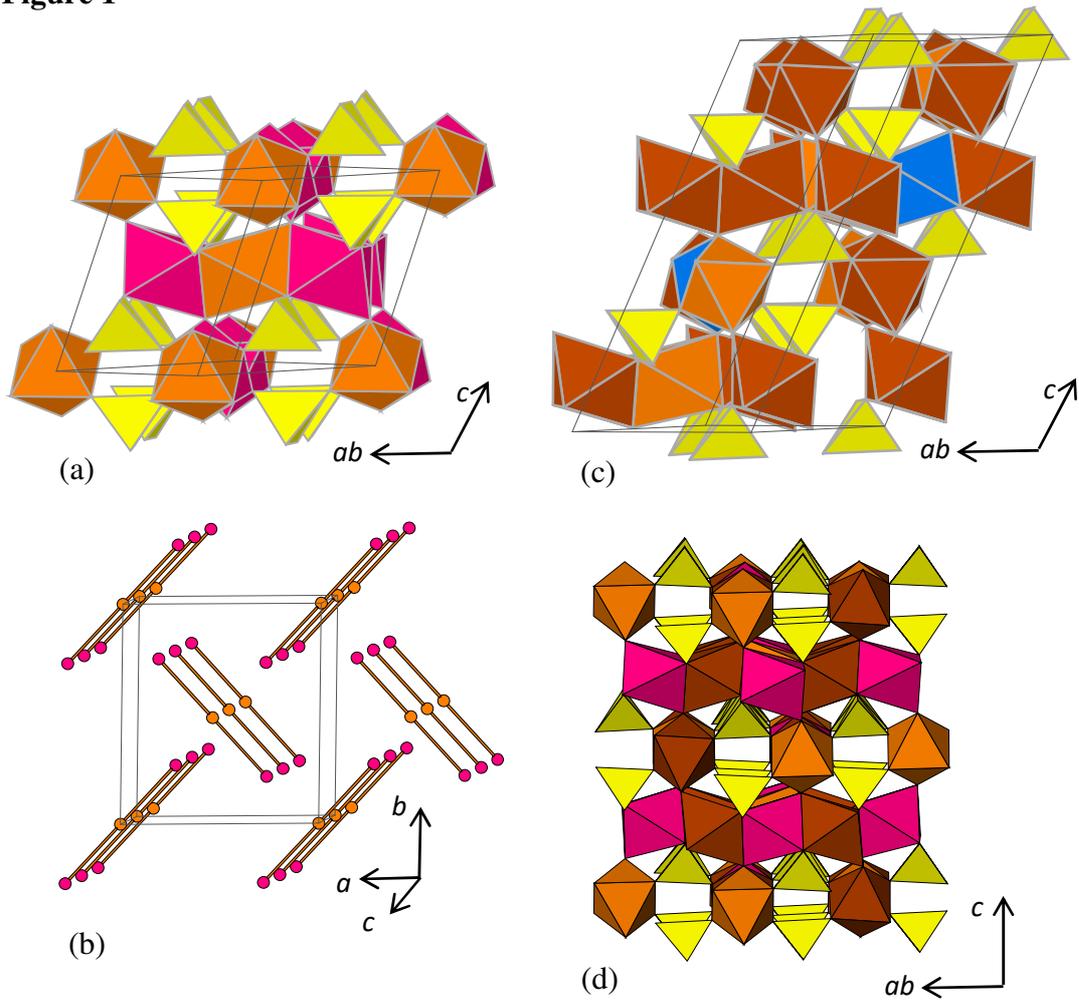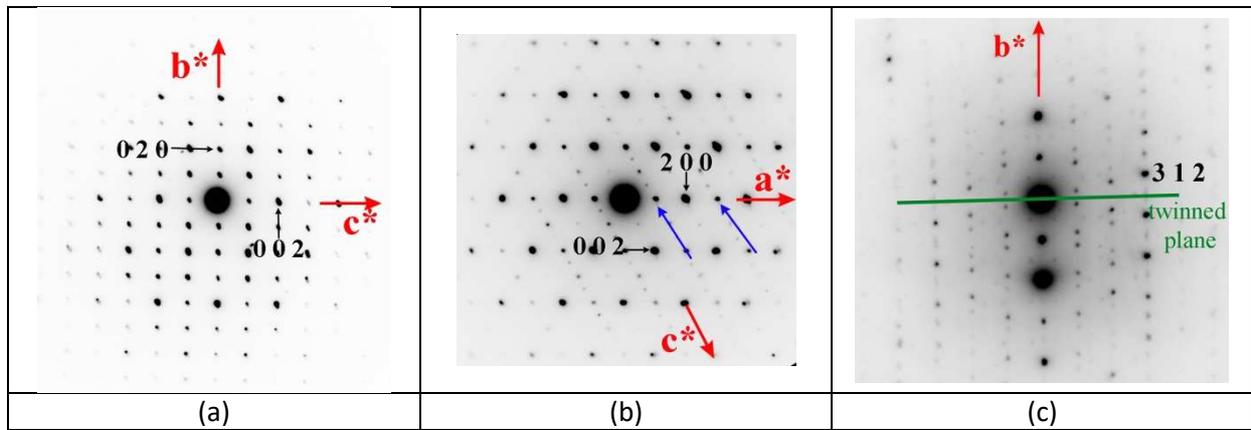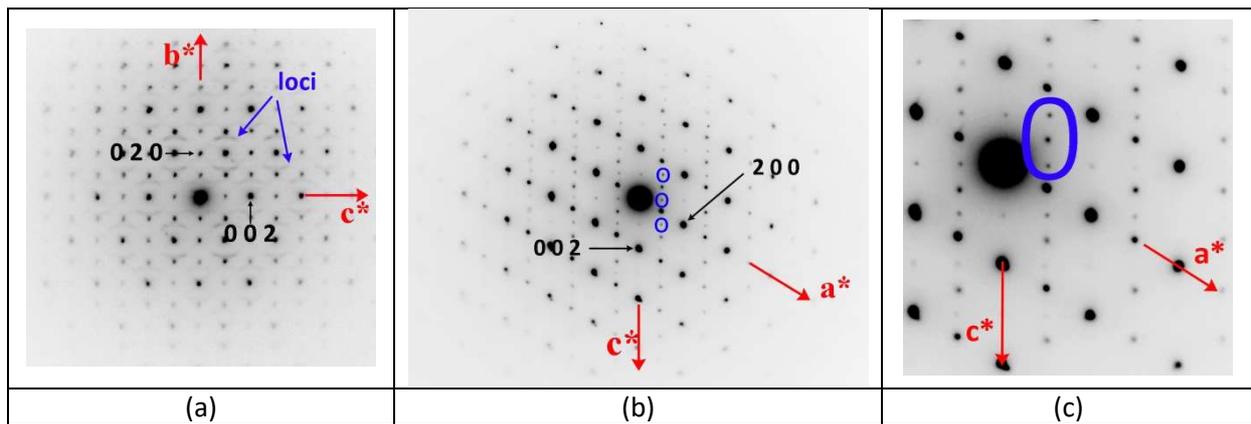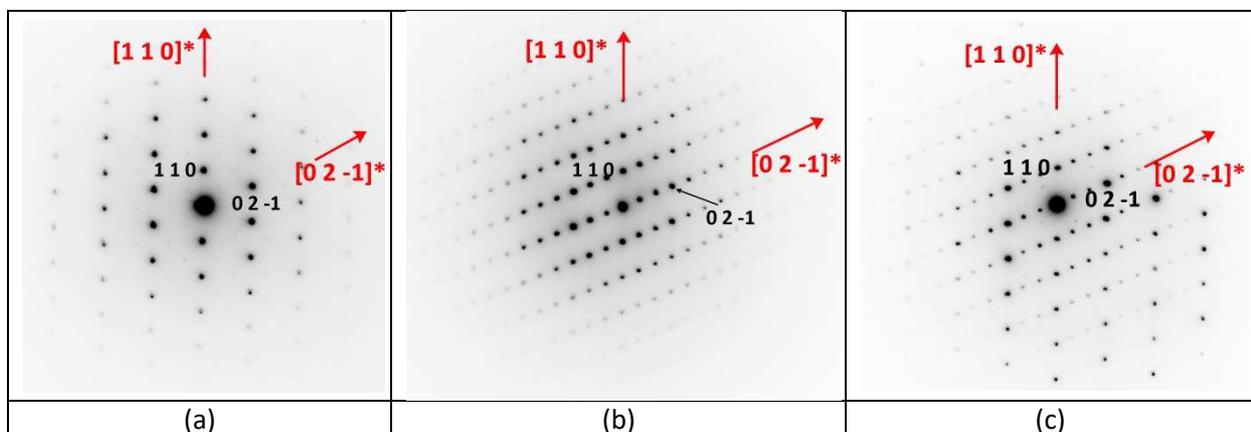
Figure 5.

Figure 6.

Figure 7.

(a)

(b)

Figure 8.

(a)

(b)

Figure 9.

(a)

(b)